RSC Advances

ROYAL SOCIETY OF CHEMISTRY

www.rsc.org/advances

The Control of Crystallographic Texture in the Use of Magnesium as a Resorbable Biomaterial

Sumit Bahl, Satyam Suwas, Kaushik Chatterjee*

Department of Materials Engineering, Indian Institute of Science, Bangalore, India 560012

* Corresponding author: kchatterjee@materials.iisc.ernet.in; +91-80-22933408

Abstract

Magnesium and its alloys are an emerging class of resorbable materials for orthopedic and cardiovascular applications. The typical strategy underlying the development of these materials involves the control of material processing routes and the addition of alloying elements. Crystallographic texture is known to control bulk mechanical as well as surface properties. However, its role in determining properties of magnesium for implant materials has not been well studied. In this work, an extruded rod of pure magnesium was cut in multiple directions to generate samples with different textures. It was found that texture significantly affected the strength and ductility of magnesium. Corrosion rates in Hank's solution decreased with the increased presence of low energy basal planes at the surface. In vitro cell studies revealed that changes in texture did not induce cytoxicity. Thus, the control of texture in magnesium based implants could be used to tailor the mechanical properties and the resorption rates without compromising on the cytocompatibility. This study elucidates the importance of texture in the use of magnesium as a resorbable biomaterial.

Keywords: Magnesium; Resorbable biomaterials; Crystallographic texture; Mechanical properties; Corrosion; Biocompatibility

1. Introduction

There is growing interest in the development of resorbable biomaterials as they can be eliminated from the body after the intended application without the need for a secondary surgical procedure. These materials offer promising new alternative for implants used in orthopedic and cardiovascular applications. Fracture fixation requires metallic plates, screws and rods to hold the bone parts together until it is regenerated. Currently these implants are made of non-resorbable materials such as titanium and its alloys, stainless steels and Co-Cr alloys[1]. In many cases, a second surgery is performed to remove these implants after the fracture is healed. . This increases costs, morbidity at implant site, risk of infection and pain to the patient[2]. Another application of resorbable implants is coronary stents used in opening of blocked arteries, which supply blood to the heart[3, 4]. It is believed that stents are not required after a certain time as the arterial wall remodels and attain equilibrium due to the stresses applied by the stent. Presence of stents for prolonged periods leads to complications such as in-stent restenosis, thrombosis and require long term use of anti-thrombotic drugs which increases the risk of hemorrhage[3, 4]. Thus, it is important to develop materials that are resorbed naturally and excreted out of the body after their desired function is accomplished.

Magnesium and its alloys are an important class of resorbable metallic biomaterials for orthopedic and cardio-vascular applications[1, 3-6]. Magnesium is favored over ceramic and polymeric biomaterials as it offers a good combination of high strength, fracture toughness and elastic modulus, which closely matches that of bone. Magnesium is a part of human metabolism and is found mainly in bone tissues. Therefore, the controlled release of magnesium ions from degrading implants may not be toxic and can be easily excreted out of the body. In fact, presence of magnesium ions are reported to have a stimulatory effect on regeneration of bone tissue[7].

High corrosion rate of magnesium compared to other metals makes it suitable for resorbable applications. Although this is an advantage, the current magnesium alloys corrode in physiological conditions before the bone is fully regenerated. Implants lose their mechanical strength due to rapid corrosion leading to their failure[1, 8]. Therefore, one of the major challenges in the development of magnesium alloys for resorbable biomedical application is the control of the corrosion rate. The commonly used methods to control the corrosion rate include alloying, processing and surface treatments. Some of the widely studied alloying elements include Ca, Al, Mn, Zn, Zr, Si among others[9-12]. It has been shown that magnesium alloys processed to obtain fine grain size show an enhanced corrosion resistance[13]. Various surface modification techniques like micro-arc oxidation, alkali treatment, chemical conversion coatings, sol-gel coatings among others have been applied to improve corrosion resistance of magnesium[6, 14, 15].

Apart from corrosion, the other important requirement for an implant is mechanical properties like strength, ductility and elastic modulus. Incidentally, the corrosion as well as the mechanical properties are strongly dependent on crystallographic texture. Crystallographic texture in a polycrystalline material is defined as an occurrence of preferred orientation of grains within the material. It is widely used in numerous engineering applications to tune material properties. Texture of magnesium alloys is known to significantly affect the corrosion resistance[16, 17]. Given the anisotropy associated with its hexagonal crystal structure[18, 19](Figure 1(a)), the mechanical properties such as strength, ductility, and elastic modulus are especially sensitive to the texture of magnesium. Control of texture to tailor properties has been successfully employed in many industries, especially for automobile and aerospace applications. Although the effect of texture of on structural properties and corrosion behavior are well established, its effects, if any, on biological response to a material is poorly understood. A few

recent investigations[20-22] have been reported on the cellular response to titanium and its alloys. However, the use of texture as a tool to tune properties to optimize the performance of materials is yet to be fully exploited for biomedical applications and there are no known reports on resorbable biomaterials such as magnesium.

The aim of this study is to investigate the effect of texture on mechanical properties, corrosion behavior and biocompatibility of commercially pure magnesium for potential use in orthopedic applications. An extruded rod of pure magnesium was cut in three directions (Figure 1(b)). Thus, the samples had similar grain size distribution but different textures. The mechanical properties and corrosion resistance for the different textures were systematically characterized. Biocompatibility was evaluated by studying the effect of leached magnesium ions on mouse osteoblasts as a model for its use in orthopedic applications.

2. Materials and Methods

2.1 Material and Processing

Indigenously melted and casted magnesium was used for this work (Composition in wt % - Mg: 99.93, Al: 0.0032, Mn: 0.0128, Cu: 0.0005, Fe: 0.0017, Si: 0.0228, Ni: 0.0003). The cast billets were pre-heated at 400 °C for 2 h followed by extrusion at speed of 10 mm/sec. The cross-section after extrusion was 15 mm x 15mm equivalent to an extrusion ratio 25: 1. The extruded rod was cut in three directions, as shown schematically in Figure 1 such that the surface normal was parallel, perpendicular and at 45° with respect to the extrusion axis. These samples will be hereafter referred to as transverse, longitudinal and 45° respectively (Figure 1(b)).

2.2 Microstructure and Texture

Characterization of microstructure and texture was carried out using Scanning Electron Microscope (SEM) based Electron Back Scattered Diffraction (EBSD) technique. EBSD was carried out on ESEM-Quanta with an EBSD set-up provided by TexSEM laboratories (Draper). Analysis of data was done using TSL-OIM software version 5.2. Crystallographic texture was analyzed along three directions, namely, perpendicular, at 45° and parallel to extrusion axis for EBSD data. The samples were polished with standard metallographic techniques followed by electro-polishing using electrolyte consisting orthophosphoric acid and ethanol in 3:5 ratio (v/v). The electro-polishing was performed 3.0 V for 30 s and 1.5 V for 120 s to produce a strain free surface for EBSD examination. EBSD data was recorded with step size of 2 μm. A large number of grains were covered to account for statistic necessary for texture analysis.

2.3 Corrosion

Potentio-dynamic polarization was used to evaluate corrosion properties of the sample in Hank's solution using a potentiostat (Gill AC). The composition of the solution used was as follows: 8.00 g/L NaCl, 1.00 g/L glucose, 0.40 g/L KCl, 0.35 g/L $NaHCO_3$, 0.14 g/L $CaCl_2$, 0.10 g/L $MgCl_2$, 0.06 g/L Na_2HPO_4, 0.06 g/L KH_2PO_4, and 0.06 g/L $MgS0_4$. The samples were prepared by grinding with SiC papers up to P3000 grit followed by final polishing using 0.25 μm diamond paste to obtain mirror finish. Samples were ultrasonically cleaned in methanol and dried before beginning the test. The polarization test was conducted with Pt as counter electrode, saturated calomel as reference electrode and sample as working electrode. The sample was immersed in the corrosion media for 30 min to stabilize the potential (rest potential) before starting the polarization. The polarization was done at a scan rate of 12 mV/min from -150 mV to +1500 mV relative to the rest potential. Cathodic polarization curve of the Tafel plots was used to calculate the corrosion potential (E_{corr}) and corrosion current density (I_{corr}).

2.4 Mechanical Testing

The effect of texture on mechanical properties was studied by compression test. The samples were tested along three directions, namely, perpendicular, at 45° and parallel to the extrusion axis. The tests were conducted at a strain rate of 10^{-3} until fracture. Adequate lubrication was provided at the contact surfaces between the sample and the grip to eliminate the effect of friction.

2.5 Biocompatibility

The effect of texture on biocompatibility was studied using MC3T3-E1 sub-clone 4 (ATCC) mouse osteoblast cell line. It is a well-established osteoblast model[23]. Indirect method was used to evaluate biocompatibility. The cells were cultured in alpha-Minimum Essential

Medium (α-MEM) with 10 % (v/v) fetal bovine serum (FBS, Gibco, Life Technologies). Antibiotic penicillin-streptomycin (Sigma) was also added at 1 % (v/v) concentration. Cell were passaged with Trypsin-EDTA and subsequently sub-cultured. Cells of passage 3 were used for all the reported studies. The conditioned medium for indirect assay was prepared by immersing Mg samples in growth medium. The ratio of sample area to medium volume was kept constant at 15 µl/mm^2 for all the immersed samples. Samples were immersed in growth medium and incubated for 24 h at 37º C and 5 % CO_2. The conditioned medium was centrifuged at 5000 rpm for 30 min to remove corrosion debris. Three replicates per sample were immersed. 200 µl of cell suspension containing 5 x 10^3 cells was added to each well of a 96-well plate. The growth medium was replaced with 200 µl of conditioned medium after 24 h of seeding cells.

MTT (3-[4,5-dimethylthiazol-2-yl]-2,5- diphenyltetrazolium bromide; thiazolyl blue) assay (Sigma) was used to measure cell viability at 1 day and 3 days after adding the conditioned medium. A stock solution of 5 mg/ml was prepared by dissolving MTT powder in sterile phosphate buffer saline (PBS). A working solution was prepared by diluting the stock solution to 1 mg/ml in growth medium. 100 µl of working solution was added to each well and incubated at 37º C and 5 % CO_2 for 2 h. The dye is reduced to purple colored formazon crystals by dehydrogenase enzyme produced in mitochondria of viable cells. The crystals were dissolved by adding 150 µl of DMSO to each well and incubatefor 15 min at 37º C. The dye concentration was quantified by measuring absorbance at 570 nm using micro-well plate reader (Biotek). All data is presented as mean ± S.D. for n = 3.

Mg^{+2} concentration in conditioned medium was measured using an atomic absorption spectrometer (AAS, Thermo Scientific). A standard curve was drawn using samples containing known concentration of Mg^{+2}. The conditioned medium was diluted 75 times in ultrapure water

(Sartorius) before measurement to bring the concentration within the range of standard curve. The pH of conditioned medium was measured using a standard pH meter.

The effects of Mg^{+2} ion concentration and pH on osteoblast viability were studied. Mg^{+2} concentration was varied in growth medium by exogenous addition of known quantity of $MgCl_2$. The concentration of Mg^{+2} in medium was varied from 10^2 µg/ml to 10^4 µg/ml. Growth medium containing endogenous Mg^{+2} concentration of 20 µg/ml was used as the control. The pH of the medium was varied by adding NaOH solution. The final pH values of the medium prepared were adjusted to 8.0, 9.0, 10.0, 11.0 and 12.0. Growth medium of pH 7.4 was used as control. 200 µl of cell suspension containing 5 x 10^3 cells was added to each well. The growth medium with controlled Mg^{+2} concentration and pH was added after 24 h of seeding cells. MTT was used to measure osteoblast viability at 1 day and 3 days after replacing growth medium following the procedures as described above. All data is presented as mean ± S.D. for n = 3.

Statistical analyses were done using one-way ANOVA (analysis of variance) with Tukey's test. Differences were considered significant for $p < 0.05$.

3. Results and Discussion

3.1. Microstructure and Texture

Figure 2 presents EBSD generated oriented imaging micrograph on transverse plane. The microstructure is equi-axed with average grain size of 20 μm. The overall orientation is depicted in Figure 3 through inverse pole figures (IPF) plots. The colored lines in Figure 3 are iso-intensity contour lines. Each color is associated with a value 'N' which is normalized intensity with respect to randomly textured sample. The normalized intensity of a randomly texture sample at every point in pole figure will be '1' indicating that all orientation are present with equal probability. The values are assigned in the legend in same figure. Value of $N > 1$ indicates occurrence of preferred orientation (texture) in the sample. The IPF plots for transverse, longitudinal and 45° sample indicate that for the transverse sample the surface normal (extrusion axis) lies perpendicular to prismatic planes $(10\bar{1}0)$ and $(11\bar{2}0)$ of hexagonal crystal. This is schematically depicted in Figure 1(b), where the extrusion axis lies perpendicular to prismatic planes. In other words, the prismatic planes are parallel to surface of transverse sample. The IPF for longitudinal sample shows that the surface normal lies perpendicular to (0001) basal planes. This implies that basal planes are parallel to the surface of the longitudinal samples. The orientation of the 45° sample lies in between prismatic and basal orientations as seen in corresponding IPF (Figure 3).

Table 1 compiles the calculated volume fractions of basal and prismatic fibers for the three samples. Transverse sample has the highest volume fraction of prismatic fiber and lowest fraction of basal fiber, as the prismatic planes are parallel to its surface. Longitudinal sample has highest fraction of basal fiber and lowest fraction of prismatic fiber as the basal planes are parallel to its surface. The 45° sample has lower volume fractions of both prismatic and basal

fiber as its lies in between the prismatic and basal orientations. To summarize the texture of extruded Mg, the prismatic planes are perpendicular and the basal planes are parallel to extrusion axis as is shown schematically in Figure 1(b).

3.2. Mechanical Properties

Figure 4 presents the stress-strain plots of the compression test for the different textures. Table 2 summarizes the strength and ductility determined from the compression curves. The transverse sample exhibited the highest strength. The longitudinal and 45° samples had similar strengths but lower than that of the transverse sample. The ductility was lower for longitudinal sample than the transverse and 45° samples. Note that texture is the only variable among the three samples and therefore, underlies the differences in mechanical properties. Deformation mechanisms operating in Mg are dependent on the texture. Basal slip and $\{10\bar{1}2\}$ tensile twinning are the dominant deformation modes active in Mg. The critical resolved shear stress (CRSS) for basal slip in Mg as measured by single crystal experiments is nearly 0.75 MPa, whereas the CRSS for prismatic slip is nearly 40 MPa[24]. The CRSS for tensile twinning is reported to be 10 MPa[25]. The other deformation modes observed in Mg are prismatic/pyramidal slip and $\{10\bar{1}1\}$/ $\{10\bar{1}3\}$ compressive twinning. Prismatic and pyramidal slip are observed only above 300 °C in pure magnesium[25] although micro-compression experiments of Mg single crystals loaded along the c-axis have shown pyramidal slip activity[26]. The room temperature (RT) CRSS for compression twining is estimated to be between 100-150 MPa[25]. In light of these data, basal slip and tensile twinning seem to be the active deformation modes in RT compression of Mg.

The transverse sample was unfavorably oriented for basal slip, but suitably oriented for $\{10\bar{1}2\}$ tensile twinning. However, as the CRSS for $\{10\bar{1}2\}$ tensile twinning is higher than basal slip the transverse sample displays the highest yield strength. The longitudinal samples had an orientation slightly deviated from ideal basal. This orientation can lead to activation of basal slip. Since the basal slip has lowest CRSS among all the deformation modes, longitudinal samples have lowest yield strength. The 45° sample is also favorably oriented for basal slip and consequently has lower yield strength. The ductility of the transverse and 45° sample is higher than that of the longitudinal sample. Another important aspect is the nature of stress-strain curve, which indicates the deformation mechanism operating during the compression test. Transverse samples display low strain hardening rate initially due twinning. Twining can provide a maximum compressive strain of 0.065 above which it saturates[25]. The results of the present investigation are corroborated by reported literature. A low strain hardening rate can be seen from Figure 4 at a strain around 0.065 above which it increases. Once the twining saturates, it renders the grain toward hard orientation for basal slip leading to rapid strain hardening. At higher strains (> 0.065) the strain hardening rate increases. The transverse sample initially has a lower strain hardening rate than longitudinal sample, but increases at higher strains. As a result transverse curve superseded the longitudinal curve at strain above 0.125. A higher strain hardening rate could likely be the reason for high ductility of transverse sample. In contrast, a lower strain hardening rate might lead to reduced ductility in longitudinal sample. The nature of the flow curve of the 45° sample is similar to that of the transverse sample in the initial stages of plastic deformation. Both the curves indicate an initial low work hardening rate, which is likely due to the occurrence of twinning. As the strain increases, the twinning strain saturates and basal slip becomes the dominant deformation mechanism. The strain hardening, therefore, increases

and the curve is similar to that of the longitudinal sample at higher strain levels. However the effect of twinning on strain hardening is less pronounced in 45° sample than transverse sample. The strain hardening rate is higher for 45° sample than transverse sample. Kleiner et al. theoretically calculated the variation of twinning strain as a function of deviation from extrusion direction [19]. The twinning strain in compression decreases with deviation from the initial extrusion direction. The lesser propensity of twinning in the 45° sample accounts for the difference in strain hardening rates between 45° sample and transverse sample. The strain hardening rate in 45° sample at higher strain is lower than transverse sample and similar to longitudinal sample. Although the total strain is higher in 45° sample than the longitudinal, the net plastic strain is same as in longitudinal (~0.15) sample. Similar values of ultimate tensile strength (UTS) and plastic strain can be attributed to similar work hardening behavior of the 45° and longitudinal samples.

3.3. Corrosion Behavior

Figure 5 shows potentio-dynamic polarization plots in Hank's solution. Tafel extrapolation method was used to calculate corrosion potential E_{corr} and corrosion current density I_{corr}. The values are listed in Table 2. Resorption rates of biomedical implants in vivo is a complex phenomenon influenced by a multitude of factors including the local physiological pH, the composition of the biological milieu including salt and proteins, and transport and flow conditions, etc. Thus, although it is difficult to mimic this environment ex vivo, the corrosion rates determined by Tafel extrapolation method are widely accepted as a reliable measure of the expected resorption rates in vivo. The corrosion rate measured here varied with deviation of the sample surface normal from extrusion axis. As the deviation increased, the corrosion rate was found to decrease. The corrosion rate decreased in the following order: transverse > 45° >

longitudinal. It is generally believed that presence of close packed basal planes improves corrosion resistance because of their low surface energy[16, 17, 27]. Fu et al determined the surface energies of (0001), $(10\bar{1}0)$ and $(11\bar{2}0)$ planes of magnesium. The surface energy was lowest for basal plane (1.54 x 10^4 J/mol) and was higher for$(10\bar{1}0)$ and $(11\bar{2}0)$ at 3.04 x 10^4 J/mol and 2.99 x 10^4 J/mol, respectively[17, 28]. Table 2 also lists the volume fraction of basal fibers. The volume fraction is low for both transverse and 45° samples and thus, show high corrosion rates. Interestingly, despite having lower basal fiber volume fraction, 45° showed corrosion rate lower than transverse. This is likely due to the fact that planes parallel to 45° surface are closer to basal orientation than that for transverse sample (see IPF in figure 3). The results are in agreement with previous reports on the effect of texture on corrosion behavior of magnesium alloys. Xin et al.[16] studied the effect of texture on corrosion behavior of extruded AZ31 alloy in 3.5 wt% NaCl[16]. They observed a continuous decrease in corrosion rate with increase in volume of grain with basal orientation. Song et al.[17] predicted from theoretical studies that that the corrosion rate of (0001) planes is about twenty times lower than that for$(10\bar{1}0)$ or $(11\bar{2}0)$ prismatic planes.

3.4. BiocompatibilityTest

The effect of texture on the viability of osteoblasts was evaluated through an indirect method wherein cells were cultured in conditioned medium after exposure to the magnesium samples of different texture. Figure 6 shows the result of MTT assay at 1 day and 3 days after adding conditioned medium. At 1 day, there was no statistically significant difference between the three samples and fresh medium, which served as the control. By day 3, the cells had proliferated in all four conditions. Cell viability was significantly higher in the control compared to the three media exposed to Mg samples. However, no statistical difference was observed

among the three conditioned media. Thus, it appears that cytocompatibility was largely unaffected by the texture of magnesium.

The anodic and catholic reactions that occur during corrosion of magnesium are as follows:

Anodic: $Mg \longrightarrow Mg^{+2} + 2e^-$

Cathodic: $2H_2O + 2e^- \longrightarrow H_2 + 2OH^-$

Corrosion leads to simultaneous increase in Mg^{+2} concentration and the pH of the medium due to formation of OH^- ions. The pH values of the all three conditioned media were similar at 8.0 (Table 4). The values of magnesium concentration present in the media conditioned for 24 h measured by AAS are also listed in Table 4. There was no statistically significant difference in concentration among the three samples. Theoretically, transverse and longitudinal samples should have much higher corrosion rates than longitudinal sample. However, there was no measurable difference in the Mg^{+2} concentration when the samples were conditioned in growth medium. $Mg(OH)_2$ along with other salts will precipitate following Mg corrosion in culture medium. All such precipitates were removed by centrifugation and only dissolved Mg^{+2} ions remained in the conditioned medium for the cell studies. Moreover, an initial high corrosion rate of transverse sample might have led to formation of protective $Mg(OH)_2$ layer retarding its further corrosion. This does not however mean that Mg^{+2} concentration stabilized after 24 h. Mg^{+2} concentration will increase with time but the rate will be slower due to presence of partially protective $Mg(OH)_2$ layer. Conditioned medium was extracted after 24 h to compare the effect of texture on biocompatibility. The conditions are likely to be different in vivo due to presence of dynamic conditions where the corrosion products will be transported away by biological fluids.

Therefore, it is important to note here that Mg^{+2} concentration in the conditioned medium should not be considered as a true measure of resorption rate. Corrosion rate determined by the Tafel extrapolation method is a more reliable indicator of the resorption rate.

The results observed for the biocompatibility tests were investigated further. Immersion of magnesium in growth medium leads to aqueous corrosion. It is possible that either of increased Mg^{+2} and pH in conditioned medium affected cell viability. The individual effects of Mg^{+2} concentration and pH on osteoblast viability was studied. Growth medium was replaced with medium having known Mg^{+2} concentration and pH. Its effect on osteoblast viability was measured at 1 day and 3 days to compare with effect of conditioned medium on viability at 1 days and 3 days respectively. Figure 7 (a) shows the effect of Mg^{+2} on cell viability at 1day and 3days after replacing growth medium with medium having known concentration of Mg^{+2}. The concentration was varied from 20 µg/ml (growth medium) to 10^4 µg/ml. It was observed that at 1 day the cell viability was not affected for up to 4 x 10^3 µg/ml Mg^{+2} concentration. On the other hand, 10^4 µg/ml concentration was found to be toxic as all the cells died within 1 day. Cell were able to proliferate at all concentrations lower than 10^4 µg/ml. However, the proliferation rate decreased with an increase in concentrations. The cell viability was statistically similar to control at concentration up to 750 µg/ml but lower at higher concentrations. Thus, concentration of Mg^{+2} up to 4 x 10^3µg/ml are mildly toxic to osteoblasts although the effect is inhibited cell growth. Extremely high concentration (> 10^4 µg/ml) is toxic to osteoblasts. Hallab et al. found Mg mildly toxic to MG-63 cells at 50 mM (1250 µg/ml) Mg^{+2} concentration[29].

The effect of pH on cell viability and proliferation is shown in Figure 7 (b). It was observed that after 1 day the cell viability was statistically similar to that in control (pH = 7.4) up to pH 9.0. The cell viability was significantly lower than control for pH 10.0, whereas all the

cells died at pH greater than 10.0. By 3 days the cells proliferated at all pH levels except pH 11.0 and 12.0 as all the cells had died within 1 day. However, the proliferation rate slowed with an increase in pH. The cell viability at 3 days was statistically similar for control and pH 8.0, but was statistically lower than control for higher pH values. Thus, these data indicate that although higher pH (< 10) inhibits cell growth, it is not cytotoxic. However, extremely high pH (> 10) leads to complete cell death. The results are in agreement with work of Gu et al where, extracts of binary Mg alloys with pH around 8.8 did not significantly reduce the viability significantly of MC3T3-E1 osteoblasts[9]. From the results of pH experiment (Figure 7 (b)), it can be said that it did not play a role in slowing the cell growth at 3 days for all the three samples. The Mg^{+2} concentration in all three conditioned medium extracted after 24 h of sample immersion was around 800 µg/ml . This value is below the limit which can retard osteoblast proliferation (Figure 7(a)). However, the observed slower proliferation rates in the samples than control could likely be the combined effect of relatively higher pH and Mg^{+2} concentration. It must be noted that the biocompatibility test in this study were based on an indirect assay in static culture. The implants in the human body experience a more complex and dynamic environment. The body fluids will transport both precipitated Mg salts as well as dissolved Mg^{+2} ions away from implant site. The cytocompatibility will be influenced by the transport of corrosion products with the fluids. Therefore, further studies with animal model are warranted to fully evaluate the role of texture on biocompatibility of magnesium implants.

Few studies have reported on the effect of crystallographic texture on the performance of biomaterials. Faghihi et al.[22] showed that texture of Ti-6A-4V alloy affects osteoblast attachment and proliferation through changes in surface energies. In another study, Hoseini et al. [21] found that higher number of Ti-OH bonds are facilitated by presence of close packed planes which

indeed improved cell material interaction. In a recent study, we reported a systematic study on the role of texture in controlling the mechanical properties, corrosion behavior and osteoblast response to titanium[20]. Even as magnesium has emerged as a promising candidate for use as a resorbable biomaterial, there is little understanding of the role, if any, of texture on its performance. From the findings of this study, it can be seen that texture influenced mechanical properties and corrosion resistance without a significant change in cytocompatibility. Thus, texture can be utilized to tune the mechanical properties and resorption rates without loss of biocompatibility while designing magnesium-based resorbable implants, in addition to other strategies such as alloying, processing and surface modification.

4. Conclusion

The effect of texture on mechanical properties, corrosion behavior and biocompatibility of pure magnesium in extruded condition was systematically evaluated. Texture significantly affected the mechanical properties. The samples taken perpendicular to extrusion direction had higher strength than the ones extracted along 45° or parallel to extrusion direction. Texture also affected ductility which was also the highest along the sample taken perpendicular to extrusion direction. The corrosion rate in Hank's solution was found to vary in the following decreasing order: transverse, at 45° and along the extrusion direction. These characteristics have been attributed to the presence of basal planes at the surface, which varies with texture and in turn controls the corrosion rates. Resistance to corrosion could be scaled with increasing fraction of grains with basal planes parallel to surface. On the other hand, for pure Mg, biocompatibility was found to be less sensitive to texture. Taken together, this study suggests that the mechanical properties and resorption rates of magnesium implants may be tuned through control of texture without loss of biocompatibility. Although texture has been utilized to improve properties of Mg as structural material, this is the first comprehensive study demonstrating its application to modulating properties of Mg for use as a resorbable biomaterial.

Acknowledgements

This work was funded by the Department of Atomic Energy- Board of Research in Nuclear Sciences (DAE-BRNS). K.C. was supported by the Ramanujan fellowship from Department of Science and Technology (DST), India. Authors gratefully acknowledge Prof. Subodh Kumar and Mr. George Raphael for assistance with the corrosion studies and Mr. R. Deshpande for help with AAS.

References

1. M. P. Staiger, A. M. Pietak, J. Huadmai and G. Dias, *Biomaterials*, 2006, **27**, 1728-1734.
2. O. Bostman and H. Pihlajamaki, *J Trauma*, 1996, **41**, 846-849.
3. B. O'Brien and W. Carroll, *Acta Biomater*, 2009, **5**, 945-958.
4. B. Heublein, R. Rohde, V. Kaese, M. Niemeyer, W. Hartung and A. Haverich, *Heart*, 2003, **89**, 651-656.
5. F. Witte, *Acta Biomater*, 2010, **6**, 1680-1692.
6. G. Manivasagam and S. Suwas, *Mater Sci Tech*, 2014, **30**, 515-520.
7. R. W. Li, N. T. Kirkland, J. Truong, J. Wang, P. N. Smith, N. Birbilis and D. R. Nisbet, *J Biomed Mater Res A*, 2014.
8. M. B. Kannan and R. Raman, *Biomaterials*, 2008, **29**, 2306-2314.
9. X. Gu, Y. Zheng, Y. Cheng, S. Zhong and T. Xi, *Biomaterials*, 2009, **30**, 484-498.
10. Z. Li, X. Gu, S. Lou and Y. Zheng, *Biomaterials*, 2008, **29**, 1329-1344.
11. E. Zhang and L. Yang, *Mat Sci Eng A*, 2008, **497**, 111-118.
12. Y. Xin, T. Hu and P. Chu, *Acta Biomater*, 2011, **7**, 1452-1459.
13. G. Argade, S. Panigrahi and R. Mishra, *Corr Sci*, 2012, **58**, 145-151.
14. L. Zhao, C. Cui, Q. Wang and S. Bu, *Corr Sci*, 2010, **52**, 2228-2234.
15. L. Li, J. Gao and Y. Wang, *Surf Coat Tech*, 2004, **185**, 92-98.
16. R. Xin, B. Li, L. Li and Q. Liu, *Mater Design*, 2011, **32**, 4548-4552.
17. G.-L. Song, R. Mishra and Z. Xu, *Electrochem Commun*, 2010, **12**, 1009-1012.
18. J. Del Valle, F. Carreno and O. Ruano, *Acta Mater*, 2006, **54**, 4247-4259.
19. S. Kleiner and P. Uggowitzer, *Mat Sci Eng A*, 2004, **379**, 258-263.
20. S. Bahl, S. Suwas and K. Chatterjee, *RSC Adv*, 2014.

21. M. Hoseini, P. Bocher, A. Shahryari, F. Azari, J. A. Szpunar and H. Vali, *J Biomed Mater Res A*, 2013.

22. S. Faghihi, F. Azari, H. Li, M. R. Bateni, J. A. Szpunar, H. Vali and M. Tabrizian, *Biomaterials*, 2006, **27**, 3532-3539.

23. H. Sudo, H.-A. Kodama, Y. Amagai, S. Yamamoto and S. Kasai, *J Cell Biol*, 1983, **96**, 191-198.

24. W. Hutchinson and M. Barnett, *Scripta Mater*, 2010, **63**, 737-740.

25. A. Chapuis and J. H. Driver, *Acta Mater*, 2011, **59**, 1986-1994.

26. C. M. Byer, B. Li, B. Cao and K. Ramesh, *Scripta Mater*, 2010, **62**, 536-539.

27. M. Hoseini, A. Shahryari, S. Omanovic and J. A. Szpunar, *Corros Sci*, 2009, **51**, 3064-3067.

28. B.-Q. Fu, W. Liu and Z.-L. Li, *Appl Surf Sci*, 2009, **255**, 9348-9357.

29. N. J. Hallab, C. Vermes, C. Messina, K. A. Roebuck, T. T. Glant and J. J. Jacobs, *J Biomed Mater Res*, 2002, **60**, 420-433.

Table 1 Volume fractions of (0001) basal fiber, $(10\bar{1}0)$ and $(11\bar{2}0)$ prismatic fibers for transverse, longitudinal and 45 samples.

Sample	**Volume fraction of fibers**		
	(0001)	$(10\bar{1}0)$	$(11\bar{2}0)$
Transverse	0.1	18.9	19.5
Longitudinal	8.2	1.0	1.0
45°	0.1	5.6	6.7

Table 2 Yield strength, ultimate tensile strength and ductility values for transverse, longitudinal and 45° samples.

Sample	Yield Strength (MPa)	Tensile Strength (MPa)	Ductility (%)
Transverse	46	275	18
Longitudinal	37	211	16
45°	43	213	19

Table 3 Corrosion current density I_{corr} and corrosion potential E_{corr} in Hank's solution measured by Tafel extrapolation

Sample	**Corrosion potential E_{corr} (mV v/s SCE)**	**Corrosion current density I_{corr} (mA/cm^2)**	**Basal fiber volume fraction (%)**
Transverse	-1667	0.16	0.1
Longitudinal	-1645	0.05	8.2
45°	-1631	0.10	0.1

Table 4 pH and Mg^{+2} concentration in conditioned medium

Sample	pH of the conditioned media	Mg^{+2} concentration in conditioned media (µg/ml)
Transverse	8.1 ± 0.1	766.0 ± 90.0
Longitudinal	8.2 ± 0.1	850.0 ± 53.5
45°	8.1 ± 0.1	837.5± 76.7

Figure captions

Figure 1. Schematic diagram of (a) hexagonal unit cell of magnesium with basal and prismatic planes (b) orientation of unit cell in extruded rod and orientations of transverse, longitudinal and 45° samples

Figure 2. EBSD micrograph on the surface of transverse sample along with stereographic triangle

Figure 3. Inverse pole figures for transverse, longitudinal and 45° samples

Figure 4. Stress-strain curves of compression tests for transverse, longitudinal and 45° samples

Figure 5. Potentio-dynamic polarization plots in Hank's solution

Figure 6. Absorbance values of MTT assay at 1 day and 3 days. * represent statistically significant difference ($p<0.05$) at 3 days.

Figure 7. Absorbance values of MTT assay at 1 day and 3 days for (a) effect of Mg^{+2} concentration (b) effect of pH, on cell viability. * and & represent statistically significant difference ($p<0.05$) at 1 day and 3 days, respectively.

Figure 1

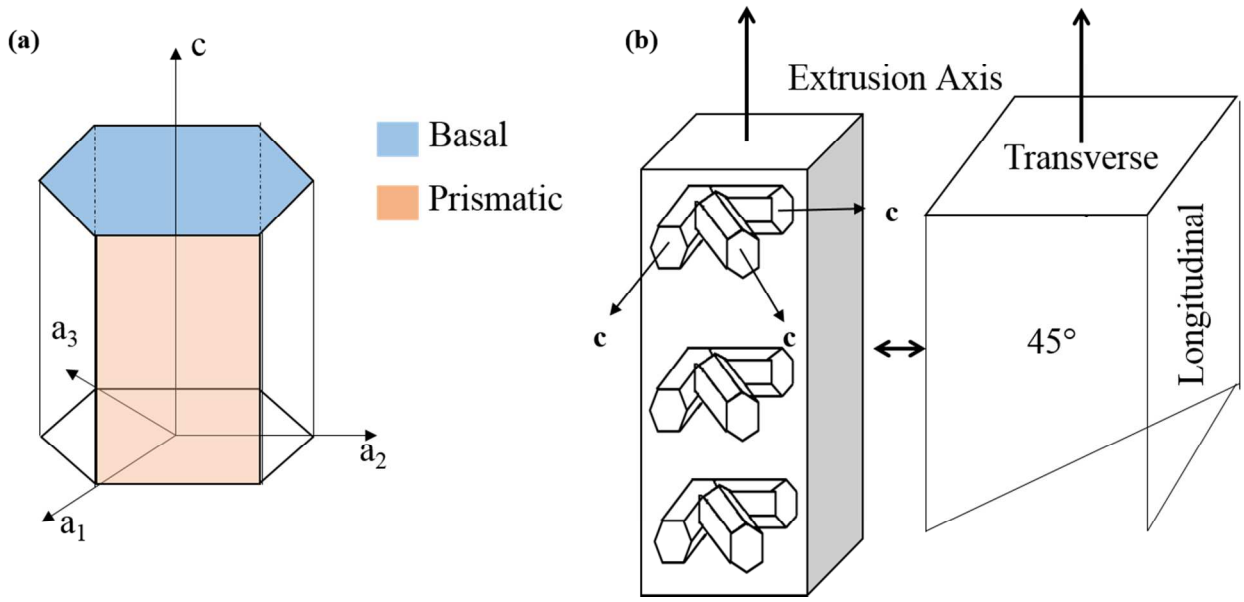

Figure 2

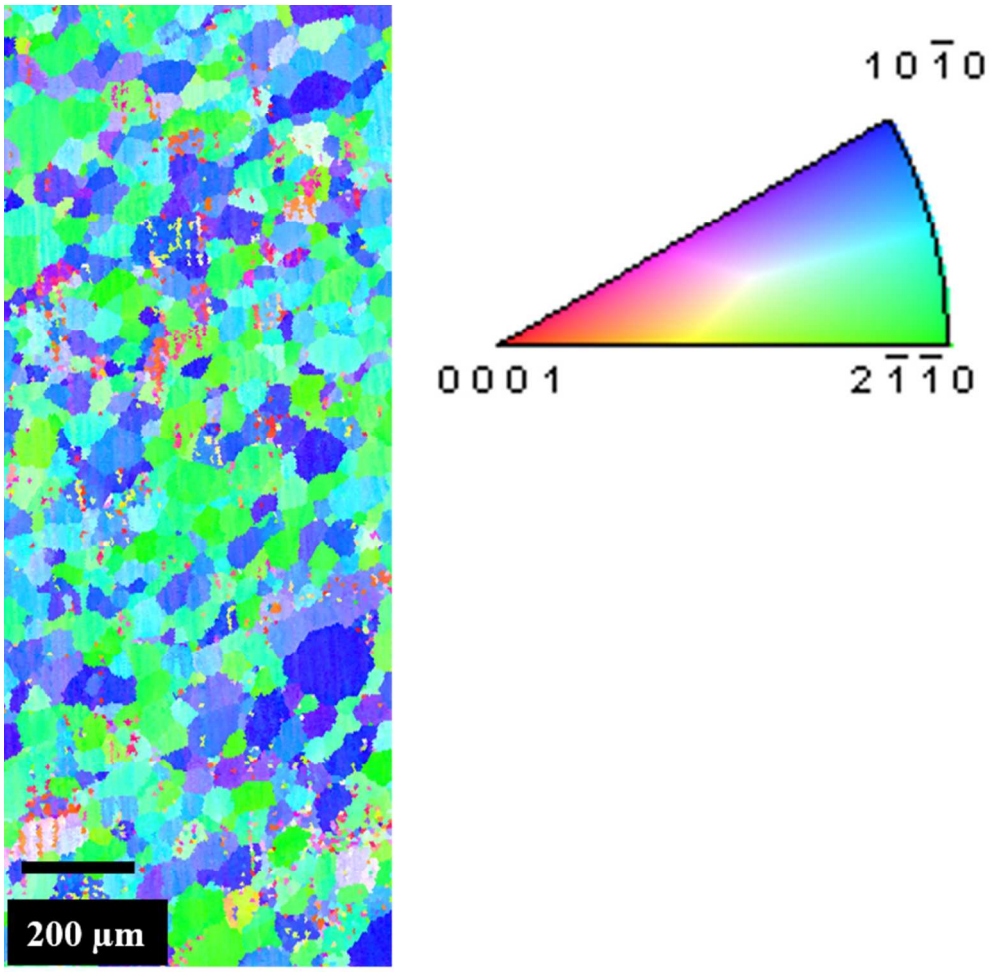

Figure 3

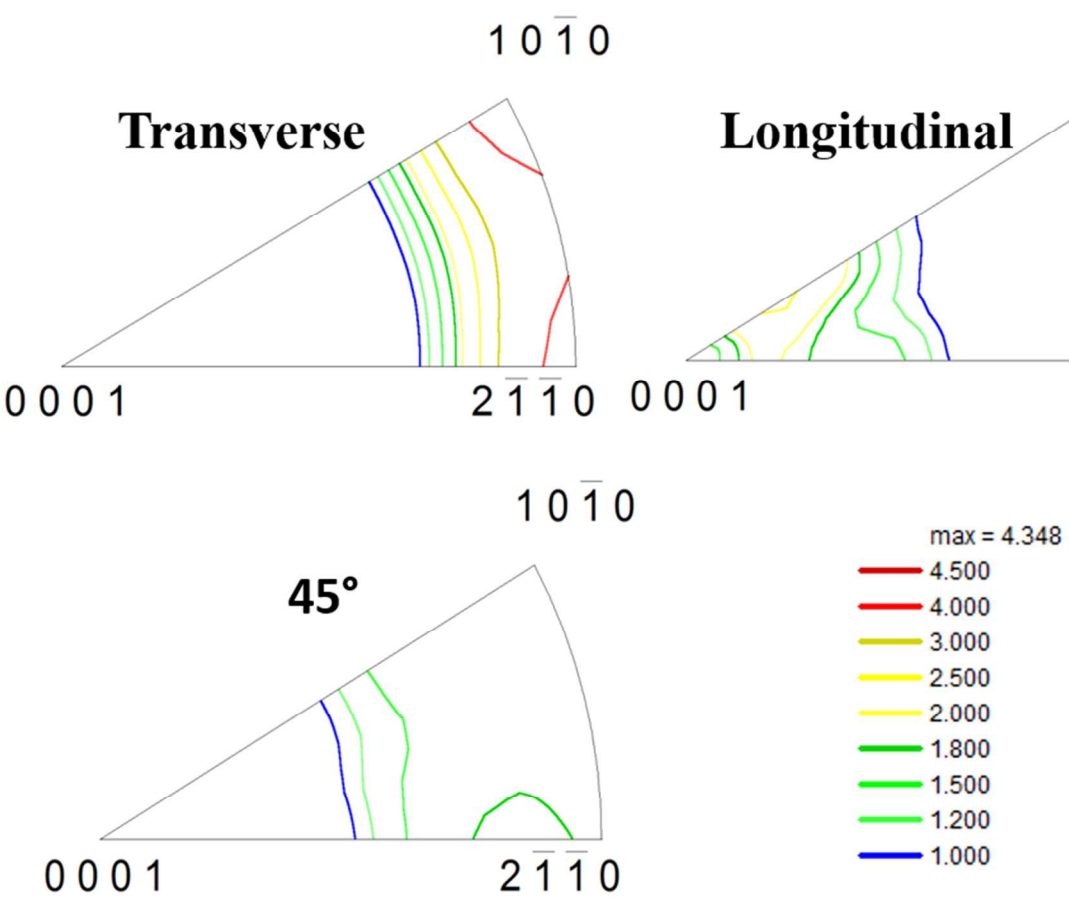

Figure 4

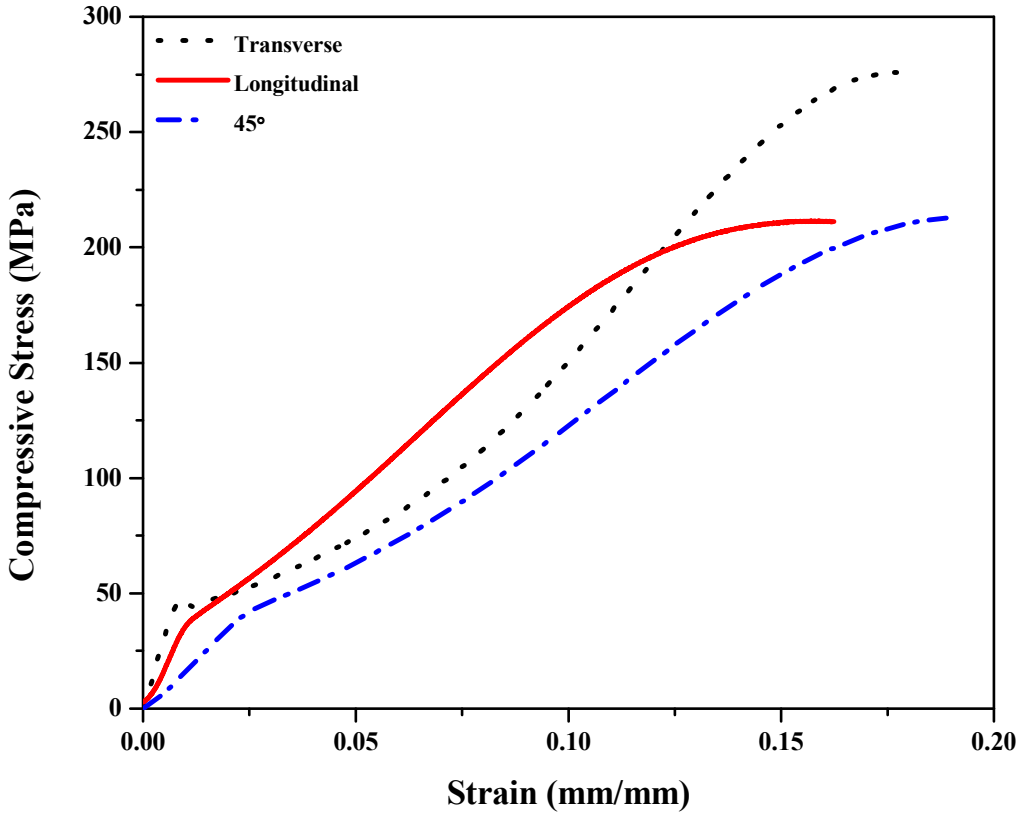

Figure 5

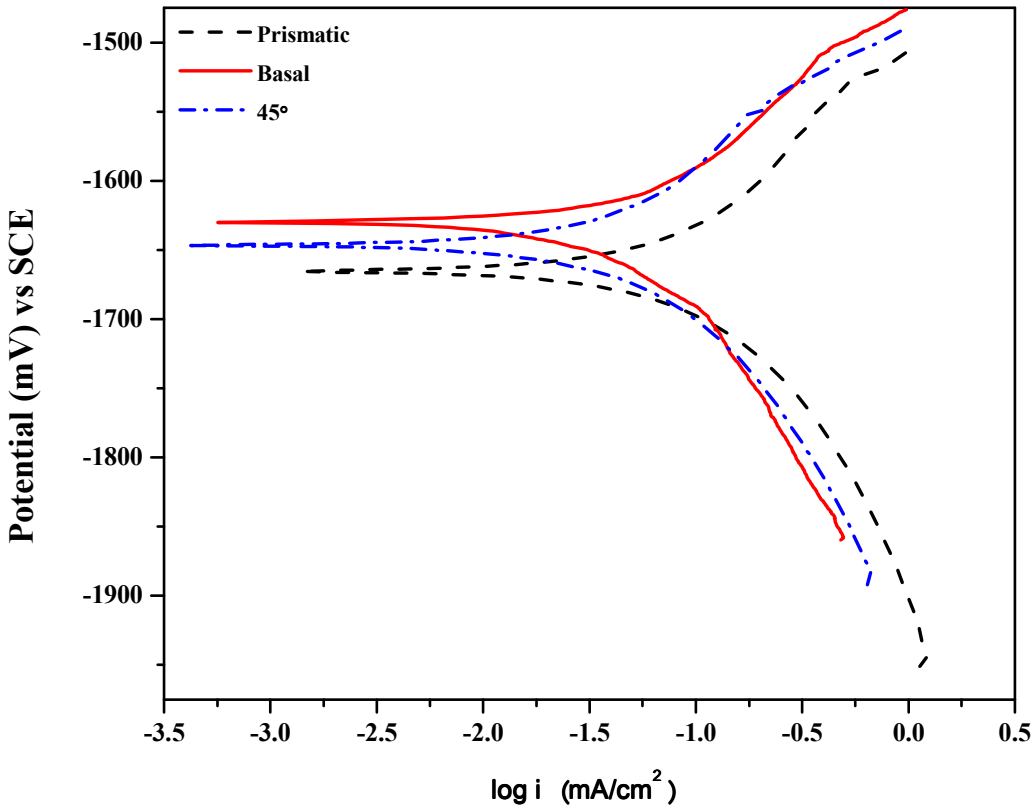

Figure 6

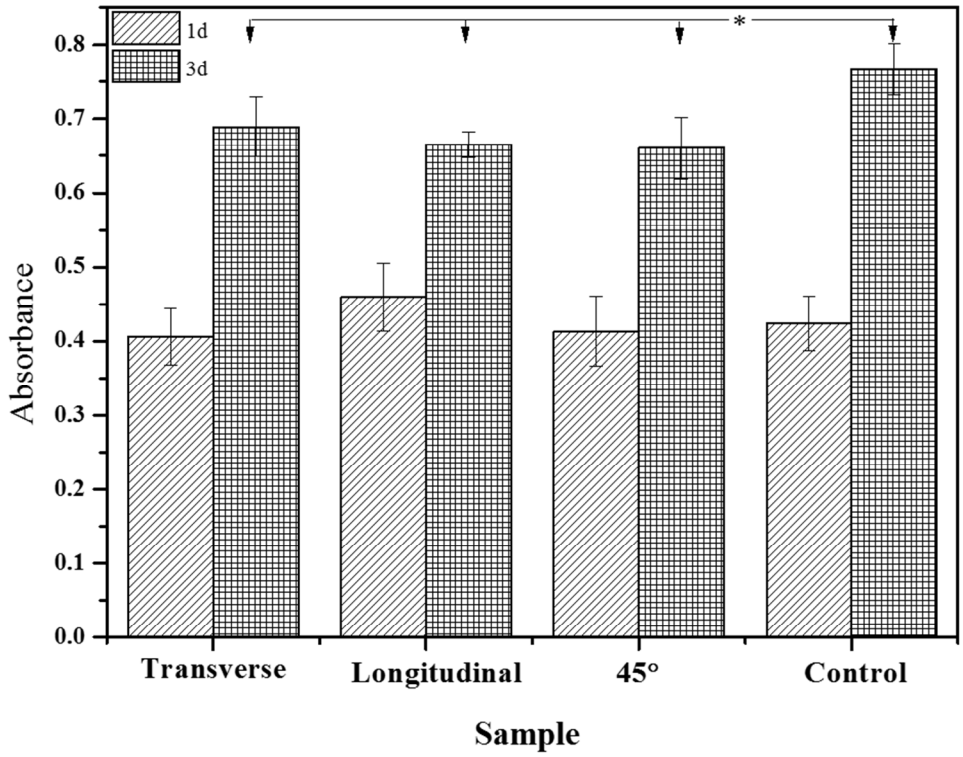

Figure 7